NANO LETTERS

pubs.acs.org/NanoLett Letter

Full-Color Quasi-Achromatic Imaging with a Dual-Functional Metasurface

Xiaomin Du, Wenjing Shen, Jian Li, Yanhao Chu, Jiacheng Sun, Junyi Wang, Jitao Ji, Chen Chen,* Shining Zhu, and Tao Li*

Cite This: https://doi.org/10.1021/acs.nanolett.5c00695 Read Online

ACCESS | Metrics & More | Article Recommendations | Supporting Information

ABSTRACT: Achieving broadband achromaticity in the visible spectrum is critical for enhancing the imaging performance of metalenses. However, many previous studies remain constrained by small device sizes or small numerical aperture. In this study, we propose a polarization-multiplexed metalens capable of generating zero- and high-order Bessel beams to achieve quasi-achromatic correction without size limitations. An image subtraction method with the two polarization channels is developed to mitigate the Bessel beam sidelobes to improve imaging quality. Our results demonstrate an effective quasi-achromatic focusing and imaging over a continuous wavelength range of 450−700 nm with long focus depth. The image subtraction method significantly enhances the image clarity and contrast, providing new insights for full-color imaging and detection.

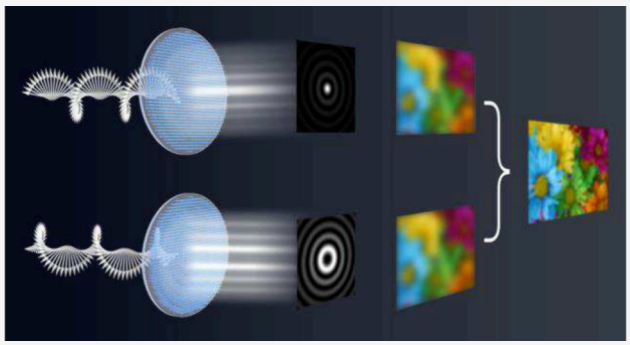

KEYWORDS: *metalens, Bessel beam, quasi-achromatic imaging, image subtraction*

Chromatic aberration in lenses causes light of different wavelengths to fail to focus on the same plane, resulting in image blurring and color distortion. Correcting chromatic aberration over a wide bandwidth is essential for achieving full-color imaging. However, traditional refractive achromatic elements (e.g., doublet lens) are typically large, costly, and challenging to manufacture with high precision. These limitations hinder their ability to satisfy the rapid development of lightweight and integrated optical devices, restricting their application in portable, wearable, and integrated systems. Metalenses are novel diffractive lenses composed of sub-wavelength unit structures with an ultrathin architecture. They also provide more precise and efficient wavefront control,[1−13] offering solutions for compact and lightweight achromatic optical elements. To date, a number of works have achieved multiwavelength achromatic metalenses, eliminating chromatic aberration at several discrete wavelengths[14−18] or within a certain continuous bandwidth.[19,20] But these limited achromatic capabilities are insufficient for full-color imaging applications. Recently, several works have achieved broadband achromatization,[21−33] but it is still constrained by the fundamental limitations of achromatic metasurfaces,[34] such as small scale, low numerical aperture (NA), and low focusing efficiency. Currently, deep learning is being increasingly applied in micro−nano optics, achieving effective chromatic aberration correction in the visible spectrum.[35−38] Although they provide significant improvement for low-quality imaging, achieving high performance through new types of optical elements or approaches is still in high demand.

To overcome the limit of large-scale achromatism, Bessel beams have gained attention due to their long depth of focus and nondiffracting properties.[39] Their unique point spread function (PSF) exhibits high stability across different focal depths, effectively addressing chromatic aberration and image blurring caused by the focal shift, making them a feasible solution for eliminating chromatic aberration in optical imaging systems. However, even so, the sidelobes of Bessel beams inevitably degrade imaging performance, leading to a decrease in the resolution and contrast. Therefore, post-processing techniques are required for optimization. Traditional deconvolution methods, such as Wiener filtering, are prone to introducing additional noise,[35,40] while deep learning approaches are inefficient due to their high computational resource requirements.[41] In contrast, the image subtraction method has gained increasing attention due to its practical feasibility and simplicity and mainly been applied in fluorescence light-sheet microscopy to eliminate sidelobe-

Received: January 31, 2025
Revised: April 15, 2025
Accepted: April 15, 2025

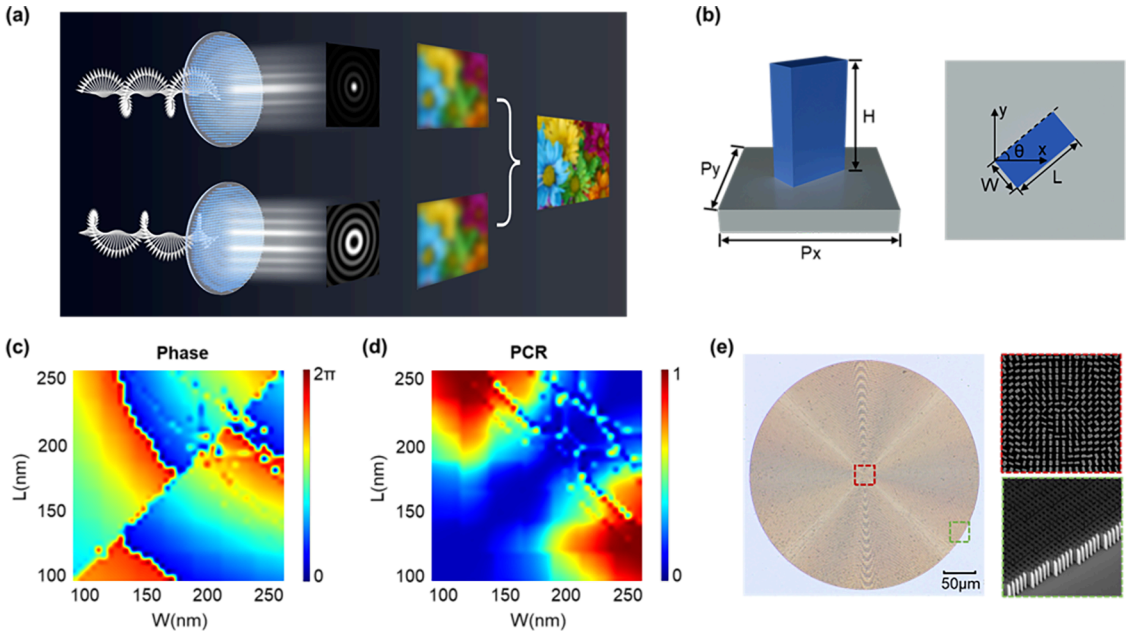

Figure 1. Imaging process and design of a polarization-multiplexed metalens. (a) Schematic illustration of the imaging principle based on the proposed polarization-multiplexed metalens. (b) Side and top views of a single nanofin. (c, d) Simulated variations of phase and polarization conversion efficiency of the transmitted optical field with size. (e) Microscopic image of the metalens and SEM images.

induced blurring,[42−49] which inspires us in improving the performance of Bessel beam based quasi-achromatic imaging.

In this study, we design a polarization-multiplexed metalens with phase profiles to generate zero- and high-order Bessel beams, which is utilized to access the long focal depth and quasi-achromatic far-field imaging in the visible region. Here, the zero-order and high-order Bessel beams are conveniently obtained by switching the polarization state of the incident light, ensuring precise overlap of their images and avoiding misalignment issues. Being imaged by both beams, full-color object images are performed with an intensity subtraction process, and sidelobe interference is then effectively suppressed. This method results in significant enhancement in image clarity and resolution, achieving high-quality full-color imaging across a broad bandwidth of 450−700 nm.

In subtraction imaging, solid and hollow beams are used to image the same object, respectively; more details of this method are provided in Supporting Information Note I. In this study, we choose the zero-order and high-order Bessel beams, and the target phase can be written as

$$\varphi(x, y) = 2\pi - \frac{2\pi}{\lambda}\sqrt{x^2 + y^2}\,NA + n\phi \tag{1}$$

where x and y represent the coordinates within the plane, NA is the numerical aperture, and the term $n\phi$ represents the vortex phase to generate high-order Bessel beams, where $\phi = \arctan(y/x)$ is the azimuthal angle.[50,51] Here, we set $NA_{zero\text{-}order} = NA_{high\text{-}order} = 0.2$ and choose $n_{zero\text{-}order} = 0$ and $n_{high\text{-}order} = 2$ to ensure that the sidelobes of the zero-order and high-order Bessel beams overlap.

To eliminate the blur caused by the sidelobes, it is necessary to precisely align the images of the 0-order and 2-order in experiments. However, mechanical methods for moving lenses usually lead to positional misalignment. Therefore, we designed a polarization-multiplexed metalens for image subtraction, with a schematic diagram of the system shown in Figure 1(a). The upper and lower rows in the figure represent the quasi-achromatic imaging processes of the zero- and high-order Bessel beams under incoherent illumination, respectively. By switching the polarization state of the incident light, the PSFs or images of the two beams can be generated at the same position on the same focal plane without the need for spatial adjustments of the lens. We selected circular polarization as the orthogonal basis, with the 0 and 2 orders of Bessel beams corresponding to right-handed circular polarization (RCP) and left-handed circular polarization (LCP), respectively. The Jones matrix of the nanofin in a metasurface describing the relation between the input electric field (E_{in}) and the output electric field (E_{out}) in a circular base can be written as[52−57]

$$J = R_c(-\theta)\begin{bmatrix} e^{i\phi_{RR}} & e^{i\phi_{RL}} \\ e^{i\phi_{LR}} & e^{i\phi_{LL}} \end{bmatrix} R_c(\theta) = \begin{bmatrix} e^{i\phi_{RR}} & e^{i(2\theta+\phi_{RL})} \\ e^{i(-2\theta+\phi_{LR})} & e^{i\phi_{LL}} \end{bmatrix} \tag{2}$$

where R_c is the rotation matrix in a circular base. In this design, we used rectangular silicon nitride (SiN_x) nanofins with a height of 1200 nm. Due to the mirror symmetry, $\phi_{LR} = \phi_{RL} = \phi$. In this work, we set the RCP-to-LCP channel to generate a 0-order Bessel beam and the LCP-to-RCP channel to generate a 2-order Bessel beam. Then the phases of the two beams can be given by $\varphi_{0\text{-}order} = 2\theta + \phi$ and $\varphi_{2\text{-}order} = -2\theta + \phi$, where θ is the rotation angle of the nanofins. Using the finite-difference time-domain (FDTD) method, we scanned the geometric and optical parameters of the nanofins on the silicon dioxide (SiO_2) substrate. Since we are interested in the broadband visible spectrum, we selected $\lambda = 530$ nm as the central design wavelength. In the simulation, periodic boundary conditions were applied in the x and y directions, and the unit cell structures of the nanofins are shown in Figure 1(b). The lattice constant for each cell was optimized as $P_x = P_y = 340$ nm, with the nanofins' length L and width W ranging from 80 to 260 nm. A library was constructed containing the geometric dimensions along with the phase and polarization conversion

https://doi.org/10.1021/acs.nanolett.5c00695
Nano Lett. XXXX, XXX, XXX−XXX

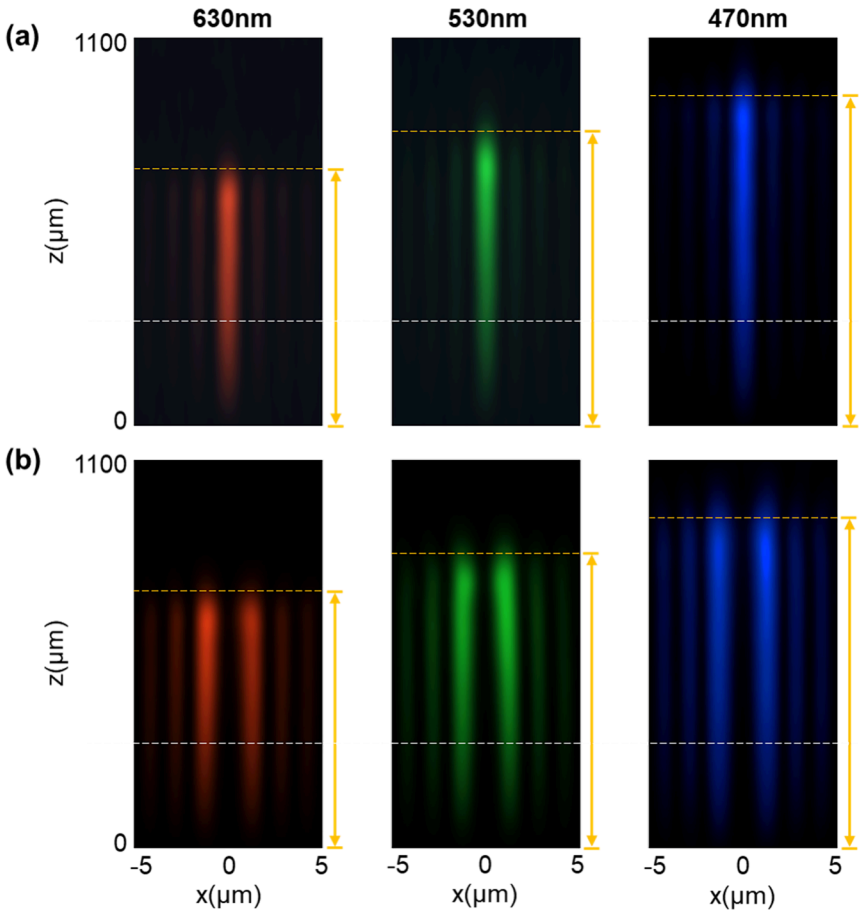

Figure 2. Longitudinal intensity distributions of Bessel beams at wavelengths of 630, 530, and 470 nm. (a) 0-order Bessel beams; (b) 2-order Bessel beams. Yellow dashed lines and bidirectional arrows indicate the position of the longest focal depth.

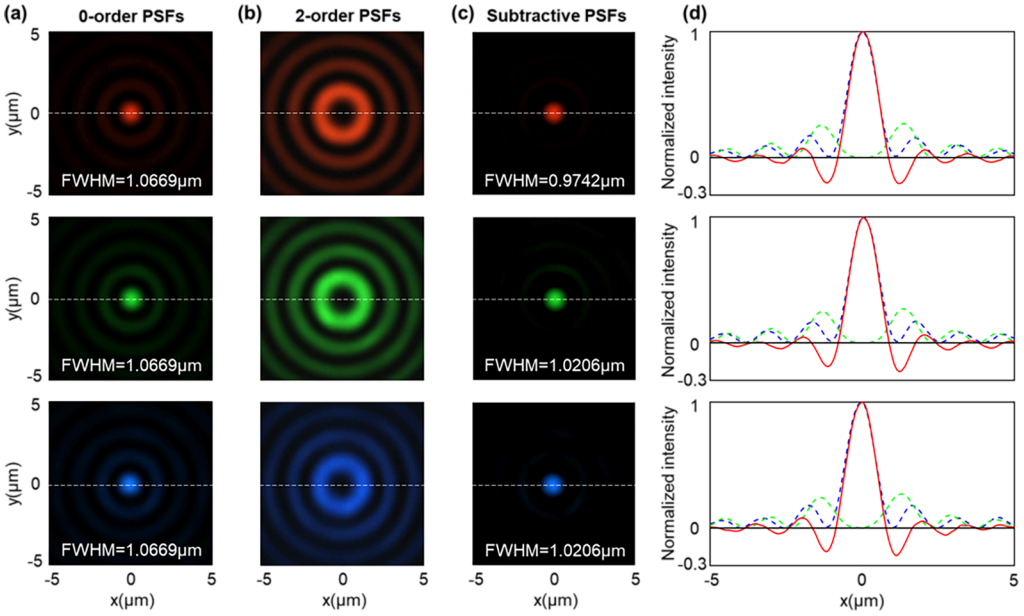

Figure 3. PSFs of Bessel beams at incident wavelengths of 630, 530, and 470 nm. (a) 0-order PSFs. (b) 2-order PSFs. (c) PSFs after subtraction with s = 0.3. (d) Normalized intensity profiles along the white dashed lines. Blue dashed lines: intensity of 0-order PSFs; green dashed lines: intensity of 2-order PSFs multiplied by 0.3; red solid lines: subtracted PSFs.

efficiencies, as shown in Figure 1(c) and Figure 1(d). The selected nanofins exhibit an average polarization conversion efficiency of up to 95% and a phase coverage ranging from 0 to 2π. The metalens was fabricated by electron beam lithography (Elionix, ELS-F125) and dry etching techniques (Oxford Instrument, Plasma Pro100 Cobra300). Figure 1(e) shows the

https://doi.org/10.1021/acs.nanolett.5c00695
Nano Lett. XXXX, XXX, XXX−XXX

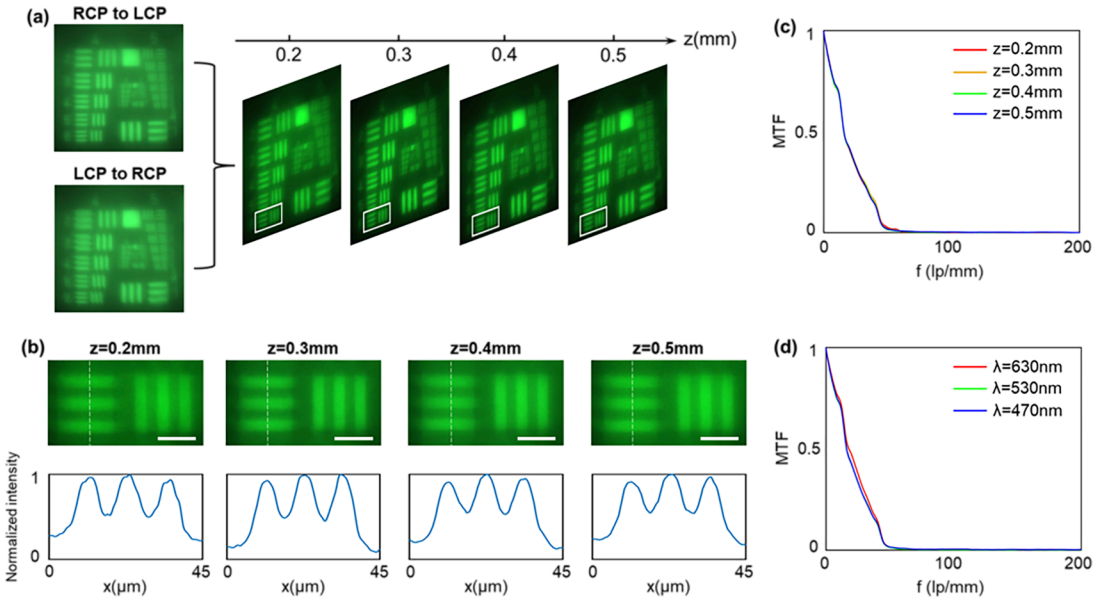

Figure 4. (a) Subtracted images at different imaging planes under 530 nm (s = 0.3). (b) Zoom-in images within the white boxes and intensity profiles along the white dashed lines. Scale bars, 20 μm. (c) MTFs of zero-order Bessel beams at different focal planes for the same wavelength (λ = 530 nm). (d) MTFs of zero-order Bessel beams at different wavelengths for the same focal plane (z = 0.3 mm).

optical microscopy image of the metalens and scanning electron microscopy (SEM) images of the nanofins. The fabricated metalens has a diameter of 350 μm. Unlike conventional achromatic metalenses, our design is not constrained by lens size and can achieve quasi-achromatic correction for larger lenses on the millimeter or even centimeter scale.

In experiments, a laser was first employed as the light source to characterize the fabricated metalens, and a CMOS camera mounted on a computer-controlled translation stage was employed to capture the PSFs of the beams. The experimental setup is shown in Supporting Information Figure S1. The longitudinal light field distributions of the 0-order (Figure 2(a)) and 2-order (Figure 2(b)) Bessel beams were measured at wavelengths of 630, 530, and 470 nm, which were extracted from a 3D field pattern reconstructed from the recorded magnified transverse field pattern slices at discrete longitudinal locations along the beam propagation direction. The position of the PSF with an intensity of 40% of the maximum PSF intensity along the z-axis is selected as the longest focal depth. More details about the determination of the longest focal depth can be seen in Supporting Information Note II. At the design wavelength, the longest focal depth of the 0-order is 858 μm, conforming to the theoretical value of the nondiffracting distance, defined as $L = \frac{D}{2\tan(\arcsin(NA))} = 857.32\ \mu$m, where the lens diameter D = 350 μm. Due to the inherent dispersion of the metalens, the longest focal depth varies with the incident wavelengths. At wavelengths of 630 and 470 nm, the longest focal depths amount to 781 and 990 μm, respectively. Notably, the longest focal depth of the 2-order Bessel beam coincides with that of its corresponding 0-order counterpart at the same wavelength. These positions are marked with yellow dashed lines and bidirectional arrows in Figure 2. Thus, under varying incident wavelengths, both 0 and 2 orders of magnitude Bessel beams exhibit considerable focal depths, which mitigates chromatic aberrations caused by wavelength variations of the focusing lens. Both the 0- and 2-order Bessel beams consist of a central main lobe and multiple sidelobes. The main lobe of the 0-order Bessel beam is solid, while that of the 2-order Bessel beam is annular, causing edge blurring of objects under incoherent illumination. The sidelobes around the main lobe introduce background noise, which severely degrades the image quality.

To address this issue, we employed an image subtraction method. The principle was demonstrated from the perspective of the PSF first. We extracted the PSFs at the white dashed lines in Figure 2 (z = 0.3 mm), with the results shown in Figure 3(a) and Figure 3(b). Since the sidelobes of the 0-order and 2-order PSF begin to overlap from the second sidelobe onward, the subtraction coefficient s is approximated as the ratio of the intensity of the second sidelobe of the 0-order PSF to that of the 2-order PSF, yielding a value of approximately 0.3. The 0-order and 2-order PSFs at different wavelengths were subtracted with the same subtraction coefficient, resulting in Figure 3(c). Figure 3(d) presents the normalized intensity profiles extracted along the white dashed lines of the PSFs. The intensity profiles of the 0-order and 2-order PSFs are represented by blue and green dashed lines, respectively. The intensity of the 2-order PSF was multiplied by 0.3, resulting in a value nearly equivalent to the intensity of the sidelobes of the 0-order PSF. Although the PSF centers were aligned, slight residual misalignment persisted in the spatial distribution of the sidelobes. Following subtraction, the sidelobes of the 0-order PSF are greatly suppressed, though it leads to some negative value regions, as shown by the red solid lines in Figure 3(d). These artifacts, however, minimally degrade image quality. In fact, the reduction in the full-width-at-half-maximum of the main lobe caused by the negative values sharpens the PSF's edges, enhancing overall image clarity. Although the PSFs at only three wavelengths are presented here, our design enables continuous broadband quasi-achromatic correction over a wavelength range of 450−700 nm. Additional PSF experimental results are provided in Supporting Information Figure S3.

https://doi.org/10.1021/acs.nanolett.5c00695
Nano Lett. XXXX, XXX, XXX−XXX

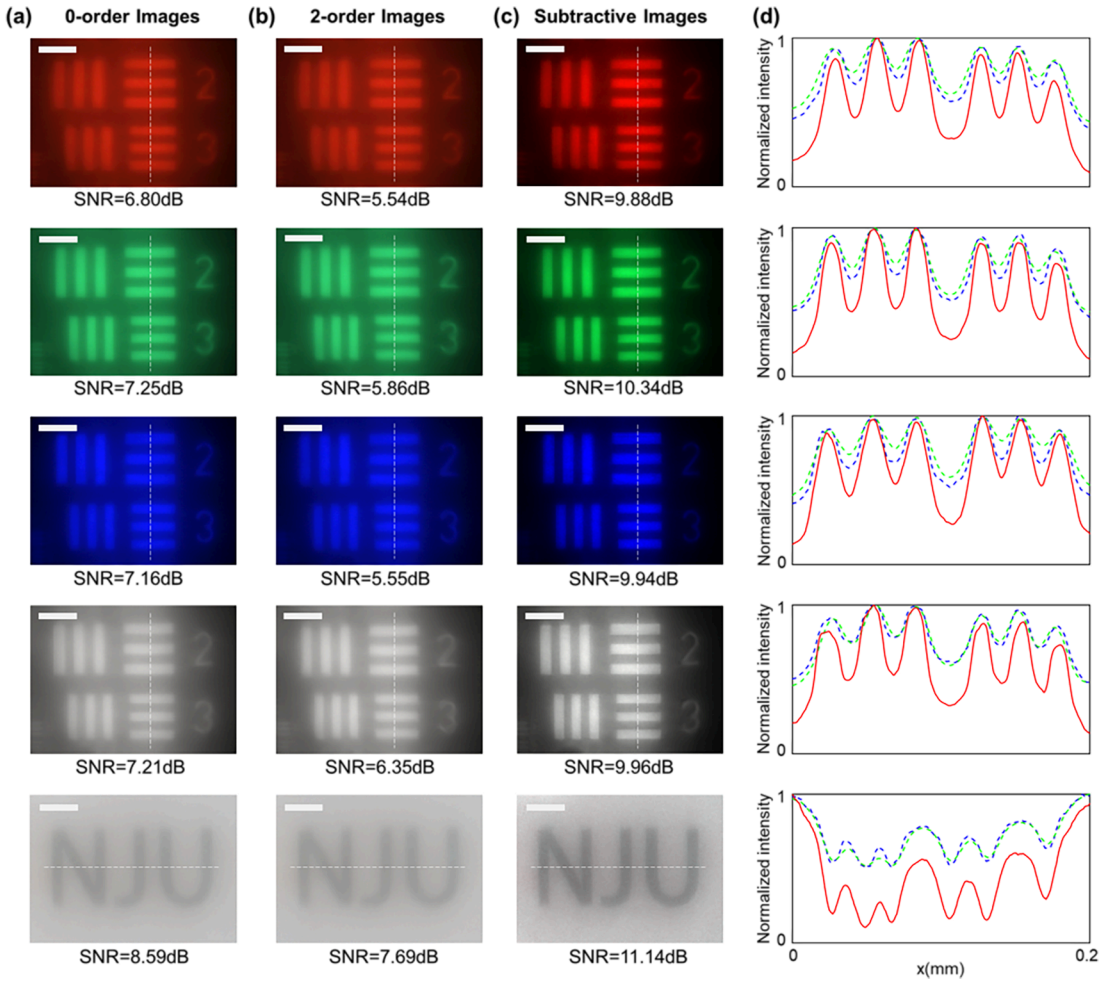

Figure 5. Experimental imaging results under 630, 530, and 470 nm and white light. (a) Images of 0-order Bessel beams. (b) Images of 2-order Bessel beams. (c) Images after subtraction with s = 0.3. Scale bars, 50 μm. (d) Normalized intensity profiles along the white dashed lines.

To verify the extended depth-of-focus imaging capability of the polarization-multiplexed metalens, we used an LED as the light source and selected the USAF1951 test chart as imaging object for the experiment. The imaging experimental setup is shown in Supporting Information Note III. It should be noted that the metalens combining a focusing phase and a spiral phase can achieve edge enhancement under coherent illumination.[58−61] However, since our design utilizes a Bessel phase, the sidelobes significantly degrade the imaging quality, making edge enhancement unattainable. In contrast, under incoherent illumination, the spiral phase causes the captured image to remain solid, but the edges become more blurred.[62,63] More simulated imaging results can be seen in Supporting Information, Note IV. Figures 4(a) and 4(b) show the imaging results of the two imaging channels and the subtraction results at different imaging planes. It can be observed that the subtractive imaging performance remains consistent across different imaging planes, indicating that the Bessel beam provides a sufficiently large working distance. We also calculated the modulation transfer function (MTF) at different focal planes for the same wavelength, as shown in Figure 4(c). The MTFs exhibit positional invariance, confirming that the Bessel beam has significant advantages in long depth imaging.

To verify the feasibility of the image subtraction method across a broad wavelength range, we first tested the imaging performance at single wavelengths with an LED light source, with the imaging object being group 3 elements 2 and 3, as the results shown in the first three rows of Figure 5. Details about the spectral bandwidth and uniformity of the LED light source are provided and discussed in Supporting Information Note III. Figure 5(a) shows the images of the 0-order Bessel beams, where it can be seen that the image is blurred at all wavelengths due to the sidelobes, but the degree of blurriness is consistent across all wavelengths. Figure 4(d) shows the MTFs at the same position for different wavelengths, which also verified the wavelength invariance. Figure 5(b) shows the images of 2-order Bessel beams; the hollow main lobe and stronger sidelobes result in increased blurriness of background. When capturing images of different polarization channels and wavelengths, we kept the camera's exposure time and gain parameters unchanged to prevent adverse pixel values resulting from dynamic changes in noise levels. And we performed an image preprocess to subtract the baseline noise caused by the ambient background. To quantitatively evaluate the quality of imaging, we defined SNR = 10 lg(I_{signal}/I_{noise}), where I_{signal} and I_{noise} refer to the intensity of the signal that can be clearly distinguished and the fluctuation of the background noise intensity, respectively.[64] The calculated SNRs at different wavelengths of 0-order and 2-order images are SNR = 6.80/5.54 dB, 7.25/5.86 dB, and 7.16/5.55 dB, respectively. The intensities of the images are subtracted, with a subtraction coefficient s = 0.3 at all wavelengths, and the final images are

https://doi.org/10.1021/acs.nanolett.5c00695
Nano Lett. XXXX, XXX, XXX−XXX

shown in Figure 5(c). Small residual misalignments (just corresponds to only a few pixels of error or even none) can be conveniently corrected using image translation functions in MATLAB. The subtracted images effectively suppress stray light compared to the original 0-order images and have a significant improvement in SNRs, which increase to 9.88, 10.34, and 9.94 dB, respectively. Compared to the 0-order PSF, the 2-order PSF has stronger sidelobe components, which results in a relatively larger intensity in the blurred background and lower image intensity in the region of interest. Therefore, by selection of an appropriate subtraction coefficient, the blurred background is suppressed, while the imaging object remains preserved. Figure 5(d) presents the normalized intensity profiles extracted along the white dashed lines, where the blue dashed line, green dashed line, and red solid line represent the image intensity profiles of 0-order, 2-order, and subtraction images, respectively. It clearly demonstrates the enhancement in clarity and contrast of the subtracted images.

Finally, imaging with different kinds of objects under broadband white light illumination was also performed to demonstrate the achromaticity. The negative resolution test chart represents the imaging situation in which the object appears bright and the background is dark. And we fabricated the letters "NJU" (an abbreviation for Nanjing University) using photolithography to represent the imaging situation in which the object appears dark and the background is bright. The last two rows in Figure 5 show the imaging results of the 0-order and 2-order beams, respectively, following the same imaging trends observed under monochromatic illumination; that is, the 2-order images appear blurrier than the 0-order images. The images of the two situations exhibit no significant chromatic aberration. The clarity of the images improves significantly after subtraction. The SNRs increase from 7.21 and 8.59 dB to 9.96 and 11.14 dB, respectively. The normalized intensity profiles along the white dashed lines are extracted, where the blue and green dashed lines represent the intensity profiles of the 0-order and 2-order beams, respectively, and the red solid lines correspond to the subtracted intensity profiles. While the subtraction operation reduces the overall image intensity, it increases the relative difference between the signal and the background without introducing additional chromatic aberration.

In summary, we proposed and experimentally demonstrated a polarization-multiplexed metalens capable of generating long focal depth Bessel beams, achieving continuous broadband quasi-achromatic imaging within the visible spectrum (450−700 nm). Experimental results showed that the image subtraction method effectively eliminates image blurring caused by Bessel beam sidelobes and significantly enhances the image clarity and contrast. Our approach overcomes the limitations of traditional achromatic metalenses in their small size and narrow bandwidth. It allows full-color imaging with a single lens and provides a longer working distance, which increases the flexibility of the optical system design. Moreover, this method is straightforward to implement and requires no complex postprocessing, making it highly suitable for real-time imaging and dynamic detection. Since our method is theoretically not limited by the lens size, it holds significant potential for large-scale quasi-achromatic imaging. This study provides a new direction for the development of compact, high-performance imaging systems with broad application potential in scientific research, medical diagnostics, and industrial inspection.

■ ASSOCIATED CONTENT

Supporting Information

The Supporting Information is available free of charge at https://pubs.acs.org/doi/10.1021/acs.nanolett.5c00695.

Principle of the image subtraction method, PSF experimental setup and the results of broadband, imaging experimental setup, imaging simulation under coherent and incoherent illumination (PDF)

■ AUTHOR INFORMATION

Corresponding Authors

Chen Chen − *National Laboratory of Solid State Microstructures, Key Laboratory of Intelligent Optical Sensing and Manipulations, Jiangsu Key Laboratory of Artificial Functional Materials, College of Engineering and Applied Sciences, Nanjing University, Nanjing 210093, China*; Email: chenchen2021@nju.edu.cn

Tao Li − *National Laboratory of Solid State Microstructures, Key Laboratory of Intelligent Optical Sensing and Manipulations, Jiangsu Key Laboratory of Artificial Functional Materials, College of Engineering and Applied Sciences, Nanjing University, Nanjing 210093, China*; orcid.org/0000-0003-0049-471X; Email: taoli@nju.edu.cn

Authors

Xiaomin Du − *National Laboratory of Solid State Microstructures, Key Laboratory of Intelligent Optical Sensing and Manipulations, Jiangsu Key Laboratory of Artificial Functional Materials, College of Engineering and Applied Sciences, Nanjing University, Nanjing 210093, China*

Wenjing Shen − *National Laboratory of Solid State Microstructures, Key Laboratory of Intelligent Optical Sensing and Manipulations, Jiangsu Key Laboratory of Artificial Functional Materials, College of Engineering and Applied Sciences, Nanjing University, Nanjing 210093, China*

Jian Li − *National Laboratory of Solid State Microstructures, Key Laboratory of Intelligent Optical Sensing and Manipulations, Jiangsu Key Laboratory of Artificial Functional Materials, College of Engineering and Applied Sciences, Nanjing University, Nanjing 210093, China*

Yanhao Chu − *National Laboratory of Solid State Microstructures, Key Laboratory of Intelligent Optical Sensing and Manipulations, Jiangsu Key Laboratory of Artificial Functional Materials, College of Engineering and Applied Sciences, Nanjing University, Nanjing 210093, China*

Jiacheng Sun − *National Laboratory of Solid State Microstructures, Key Laboratory of Intelligent Optical Sensing and Manipulations, Jiangsu Key Laboratory of Artificial Functional Materials, College of Engineering and Applied Sciences, Nanjing University, Nanjing 210093, China*

Junyi Wang − *National Laboratory of Solid State Microstructures, Key Laboratory of Intelligent Optical Sensing and Manipulations, Jiangsu Key Laboratory of Artificial Functional Materials, College of Engineering and*

https://doi.org/10.1021/acs.nanolett.5c00695
Nano Lett. XXXX, XXX, XXX−XXX

Applied Sciences, Nanjing University, Nanjing 210093, China

Jitao Ji − *National Laboratory of Solid State Microstructures, Key Laboratory of Intelligent Optical Sensing and Manipulations, Jiangsu Key Laboratory of Artificial Functional Materials, College of Engineering and Applied Sciences, Nanjing University, Nanjing 210093, China*

Shining Zhu − *National Laboratory of Solid State Microstructures, Key Laboratory of Intelligent Optical Sensing and Manipulations, Jiangsu Key Laboratory of Artificial Functional Materials, College of Engineering and Applied Sciences, Nanjing University, Nanjing 210093, China*

Complete contact information is available at: https://pubs.acs.org/10.1021/acs.nanolett.5c00695

Author Contributions

T.L., C.C., X.D., and Y.C. conceived the idea and proposed the design. X.D. performed the numerical simulation. J.L. and J.S. fabricated the samples. X.D. and W.S. performed the optical measurement with the help of J.W. and C.C. X.D., C.C., and W.S. analyzed the results with help from all authors. X.D., C.C., and T.L. wrote the manuscript with input from all authors. T.L. supervised the project.

Notes

The authors declare no competing financial interest.

■ ACKNOWLEDGMENTS

The authors acknowledge the funding provided by National Key Research and Development Program of China (2022YFA-1404301, 2024YFA1012600), National Natural Science Foundation of China (Nos. 62325504, 62305149, 92250304, 62288101), and Dengfeng Project B of Nanjing University. The authors acknowledge the microfabrication center of the National Laboratory of Solid State Microstructures (NLSSM) for technique support.

■ REFERENCES

(1) Arbabi, A.; Horie, Y.; Bagheri, M.; Faraon, A. Dielectric metasurfaces for complete control of phase and polarization with subwavelength spatial resolution and high transmission. *Nat. Nanotechnol.* **2015**, *10* (11), 937−943.

(2) Arbabi, E.; Arbabi, A.; Kamali, S. M.; Horie, Y.; Faraon, A. Multiwavelength metasurfaces through spatial multiplexing. *Sci. Rep.* **2016**, *6* (1), 32803.

(3) Eisenbach, O.; Avayu, O.; Ditcovski, R.; Ellenbogen, T. Metasurfaces based dual wavelength diffractive lenses. *Opt. Express* **2015**, *23* (4), 3928−3936.

(4) Fan, Z.-B.; Shao, Z.-K.; Xie, M.-Y.; Pang, X.-N.; Ruan, W.-S.; Zhao, F.-L.; Chen, Y.-J.; Yu, S.-Y.; Dong, J.-W. Silicon Nitride Metalenses for Close-to-One Numerical Aperture and Wide-Angle Visible Imaging. *Phys. Rev. Appl.* **2018**, *10* (1), No. 014005.

(5) Groever, B.; Chen, W. T.; Capasso, F. Meta-Lens Doublet in the Visible Region. *Nano Lett.* **2017**, *17* (8), 4902−4907.

(6) Khorasaninejad, M.; Chen, W. T.; Devlin, R. C.; Oh, J.; Zhu, A. Y.; Capasso, F. Metalenses at visible wavelengths: Diffraction-limited focusing and subwavelength resolution imaging. *Science* **2016**, *352* (6290), 1190−1194.

(7) Khorasaninejad, M.; Zhu, A. Y.; Roques-Carmes, C.; Chen, W. T.; Oh, J.; Mishra, I.; Devlin, R. C.; Capasso, F. Polarization-Insensitive Metalenses at Visible Wavelengths. *Nano Lett.* **2016**, *16* (11), 7229−7234.

(8) West, P. R.; Stewart, J. L.; Kildishev, A. V.; Shalaev, V. M.; Shkunov, V. V.; Strohkendl, F.; Zakharenkov, Y. A.; Dodds, R. K.; Byren, R. All-dielectric subwavelength metasurface focusing lens. *Opt. Express* **2014**, *22* (21), 26212−26221.

(9) Xu, H.-X.; Ma, S.; Luo, W.; Cai, T.; Sun, S.; He, Q.; Zhou, L. Aberration-free and functionality-switchable meta-lenses based on tunable metasurfaces. *Appl. Phys. Lett.* **2016**, *109* (19), No. 193506.

(10) Yu, N.; Capasso, F. Flat optics with designer metasurfaces. *Nat. Mater.* **2014**, *13* (2), 139−150.

(11) Zhou, J.; Qian, H.; Hu, G.; Luo, H.; Wen, S.; Liu, Z. Broadband Photonic Spin Hall Meta-Lens. *ACS Nano* **2018**, *12* (1), 82−88.

(12) Li, T.; Chen, C.; Xiao, X.; Chen, J.; Hu, S.; Zhu, S. Revolutionary meta-imaging: from superlens to metalens. *Photonics Insights* **2023**, *2* (1), R01.

(13) Jeon, D.; Shin, K.; Moon, S.-W.; Rho, J. Recent advancements of metalenses for functional imaging. *Nano Convergence* **2023**, *10* (1), 24.

(14) Khorasaninejad, M.; Aieta, F.; Kanhaiya, P.; Kats, M. A.; Genevet, P.; Rousso, D.; Capasso, F. Achromatic Metasurface Lens at Telecommunication Wavelengths. *Nano Lett.* **2015**, *15* (8), 5358−5362.

(15) Aieta, F.; Kats, M. A.; Genevet, P.; Capasso, F. Multiwavelength achromatic metasurfaces by dispersive phase compensation. *Science* **2015**, *347* (6228), 1342−1345.

(16) Avayu, O.; Almeida, E.; Prior, Y.; Ellenbogen, T. Composite functional metasurfaces for multispectral achromatic optics. *Nat. Commun.* **2017**, *8* (1), 14992.

(17) Hu, J.; Liu, C.-H.; Ren, X.; Lauhon, L. J.; Odom, T. W. Plasmonic Lattice Lenses for Multiwavelength Achromatic Focusing. *ACS Nano* **2016**, *10* (11), 10275−10282.

(18) Arbabi, E.; Arbabi, A.; Kamali, S. M.; Horie, Y.; Faraon, A. Multiwavelength polarization-insensitive lenses based on dielectric metasurfaces with meta-molecules. *Optica* **2016**, *3* (6), 628−633.

(19) Khorasaninejad, M.; Shi, Z.; Zhu, A. Y.; Chen, W. T.; Sanjeev, V.; Zaidi, A.; Capasso, F. Achromatic Metalens over 60 nm Bandwidth in the Visible and Metalens with Reverse Chromatic Dispersion. *Nano Lett.* **2017**, *17* (3), 1819−1824.

(20) Arbabi, E.; Arbabi, A.; Kamali, S. M.; Horie, Y.; Faraon, A. Controlling the sign of chromatic dispersion in diffractive optics with dielectric metasurfaces. *Optica* **2017**, *4* (6), 625−632.

(21) Chen, W. T.; Zhu, A. Y.; Sanjeev, V.; Khorasaninejad, M.; Shi, Z.; Lee, E.; Capasso, F. A broadband achromatic metalens for focusing and imaging in the visible. *Nat. Nanotechnol.* **2018**, *13* (3), 220−226.

(22) Wang, S.; Wu, P. C.; Su, V.-C.; Lai, Y.-C.; Chen, M.-K.; Kuo, H. Y.; Chen, B. H.; Chen, Y. H.; Huang, T.-T.; Wang, J.-H.; et al. A broadband achromatic metalens in the visible. *Nat. Nanotechnol.* **2018**, *13* (3), 227−232.

(23) Wang, S.; Wu, P. C.; Su, V.-C.; Lai, Y.-C.; Hung Chu, C.; Chen, J.-W.; Lu, S.-H.; Chen, J.; Xu, B.; Kuan, C.-H.; et al. Broadband achromatic optical metasurface devices. *Nat. Commun.* **2017**, *8* (1), 187.

(24) Sun, P.; Zhang, M.; Dong, F.; Feng, L.; Chu, W. Broadband achromatic polarization insensitive metalens over 950 nm bandwidth in the visible and near-infrared. *Chin. Opt. Lett.* **2022**, *20* (1), No. 013601.

(25) Balli, F.; Sultan, M. A.; Ozdemir, A.; Hastings, J. T. An ultrabroadband 3D achromatic metalens. *Nanophotonics* **2021**, *10* (4), 1259−1264.

(26) Ndao, A.; Hsu, L.; Ha, J.; Park, J.-H.; Chang-Hasnain, C.; Kanté, B. Octave bandwidth photonic fishnet-achromatic-metalens. *Nat. Commun.* **2020**, *11* (1), 3205.

(27) Balli, F.; Sultan, M.; Lami, S. K.; Hastings, J. T. A hybrid achromatic metalens. *Nat. Commun.* **2020**, *11* (1), 3892.

(28) Fan, Z.-B.; Qiu, H.-Y.; Zhang, H.-L.; Pang, X.-N.; Zhou, L.-D.; Liu, L.; Ren, H.; Wang, Q.-H.; Dong, J.-W. A broadband achromatic metalens array for integral imaging in the visible. *Light Sci. Appl.* **2019**, *8* (1), 67.

(29) Lin, R. J.; Su, V.-C.; Wang, S.; Chen, M. K.; Chung, T. L.; Chen, Y. H.; Kuo, H. Y.; Chen, J.-W.; Chen, J.; Huang, Y.-T.; et al. Achromatic metalens array for full-colour light-field imaging. *Nat. Nanotechnol.* **2019**, *14* (3), 227−231.

(30) Chen, W. T.; Zhu, A. Y.; Sisler, J.; Bharwani, Z.; Capasso, F. A broadband achromatic polarization-insensitive metalens consisting of anisotropic nanostructures. *Nat. Commun.* **2019**, *10* (1), 355.
(31) Li, Z.; Lin, P.; Huang, Y.-W.; Park, J.-S.; Chen, W. T.; Shi, Z.; Qiu, C.-W.; Cheng, J.-X.; Capasso, F. Meta-optics achieves RGB-achromatic focusing for virtual reality. *Sci. Adv.* **2021**, *7* (5), No. eabe4458.
(32) Xiao, X.; Zhao, Y.; Ye, X.; Chen, C.; Lu, X.; Rong, Y.; Deng, J.; Li, G.; Zhu, S.; Li, T. Large-scale achromatic flat lens by light frequency-domain coherence optimization. *Light Sci. Appl.* **2022**, *11* (1), 323.
(33) Ren, H.; Jang, J.; Li, C.; Aigner, A.; Plidschun, M.; Kim, J.; Rho, J.; Schmidt, M. A.; Maier, S. A. An achromatic metafiber for focusing and imaging across the entire telecommunication range. *Nat. Commun.* **2022**, *13* (1), 4183.
(34) Shrestha, S.; Overvig, A. C.; Lu, M.; Stein, A.; Yu, N. Broadband achromatic dielectric metalenses. *Light Sci. Appl.* **2018**, *7* (1), 85.
(35) Colburn, S.; Zhan, A.; Majumdar, A. Metasurface optics for full-color computational imaging. *Sci. Adv.* **2018**, *4* (2), No. eaar2114.
(36) Dong, Y.; Zheng, B.; Li, H.; Tang, H.; Zhao, H.; Huang, Y.; An, S.; Zhang, H. Achromatic Single Metalens Imaging via Deep Neural Network. *ACS Photonics* **2024**, *11* (4), 1645−1656.
(37) Hu, S.; Shi, R.; Wang, B.; Wei, Y.; Qi, B.; Zhou, P. Full-Color Imaging System Based on the Joint Integration of a Metalens and Neural Network. *Nanomaterials* **2024**, *14* (8), 715.
(38) Zhang, Y.; Song, X.; Xie, J.; Hu, J.; Chen, J.; Li, X.; Zhang, H.; Zhou, Q.; Yuan, L.; Kong, C.; et al. Large depth-of-field ultra-compact microscope by progressive optimization and deep learning. *Nat. Commun.* **2023**, *14* (1), 4118.
(39) Durnin, J. Exact solutions for nondiffracting beams. I. The scalar theory. *J. Opt. Soc. Am. A* **1987**, *4*, 651−654.
(40) Qin, S. Image reconstruction for large FOV Airy beam light-sheet microscopy by a 3D deconvolution approach. *Opt. Lett.* **2020**, *45* (10), 2804−2807.
(41) Stockhausen, A.; Rodriguez-Gatica, J. E.; Schweihoff, J.; Schwarz, M. K.; Kubitscheck, U. Airy beam light sheet microscopy boosted by deep learning deconvolution. *Opt. Express* **2023**, *31* (6), 10918−10935.
(42) Jia, H.; Yu, X.; Yang, Y.; Zhou, X.; Yan, S.; Liu, C.; Lei, M.; Yao, B. Axial resolution enhancement of light-sheet microscopy by double scanning of Bessel beam and its complementary beam. *J. Biophotonics* **2019**, *12* (1), No. e201800094.
(43) Deng, S.; Wang, P.; Zhang, Y.; Zhou, H.; Yang, J.; Liu, M. Subtraction method via phase mask enables contrast enhancement in scanned Bessel light-sheet microscopy. *J. Opt. Soc. Am. A* **2020**, *37* (1), 84−88.
(44) Deng, S.; Yuan, L.; Cheng, P.; Wang, Y.; Liu, M. Enhancement of image quality in planar Airy light-sheet microscopy via subtraction method. *J. Opt.* **2022**, *24* (2), No. 025301.
(45) Le, V.; Wang, X.; Kuang, C.; Liu, X. Axial resolution enhancement for light sheet fluorescence microscopy via using the subtraction method. *Opt. Eng.* **2018**, *57* (10), No. 103107.
(46) Liu, C.; Yu, X.; Bai, C.; Li, X.; Zhou, Y.; Yan, S.; Min, J.; Dan, D.; Li, R.; Gu, S.; Yao, B. Axial resolution enhancement for planar Airy beam light-sheet microscopy via the complementary beam subtraction method. *Appl. Opt.* **2021**, *60* (32), 10239−10245.
(47) Gao, P.; Nienhaus, G. U. Precise background subtraction in stimulated emission double depletion nanoscopy. *Opt. Lett.* **2017**, *42* (4), 831−834.
(48) Tian, N.; Fu, L.; Gu, M. Resolution and contrast enhancement of subtractive second harmonic generation microscopy with a circularly polarized vortex beam. *Sci. Rep.* **2015**, *5* (1), 13580.
(49) Wang, N.; Kobayashi, T. Numerical study of the subtraction threshold for fluorescence difference microscopy. *Opt. Express* **2014**, *22* (23), 28819−28830.
(50) Chen, W. T.; Khorasaninejad, M.; Zhu, A. Y.; Oh, J.; Devlin, R. C.; Zaidi, A.; Capasso, F. Generation of wavelength-independent subwavelength Bessel beams using metasurfaces. *Light Sci. Appl.* **2017**, *6* (5), e16259−e16259.
(51) Li, T.; Li, X.; Yan, S.; Xu, X.; Wang, S.; Yao, B.; Wang, Z.; Zhu, S. Generation and Conversion Dynamics of Dual Bessel Beams with a Photonic Spin-Dependent Dielectric Metasurface. *Phys. Rev. Appl.* **2021**, *15* (1), No. 014059.
(52) Balthasar Mueller, J. P.; Rubin, N. A.; Devlin, R. C.; Groever, B.; Capasso, F. Metasurface Polarization Optics: Independent Phase Control of Arbitrary Orthogonal States of Polarization. *Phys. Rev. Lett.* **2017**, *118* (11), No. 113901.
(53) Zhao, R.; Sain, B.; Wei, Q.; Tang, C.; Li, X.; Weiss, T.; Huang, L.; Wang, Y.; Zentgraf, T. Multichannel vectorial holographic display and encryption. *Light Sci. Appl.* **2018**, *7* (1), 95.
(54) Chen, C.; Gao, S.; Song, W.; Li, H.; Zhu, S.-N.; Li, T. Metasurfaces with Planar Chiral Meta-Atoms for Spin Light Manipulation. *Nano Lett.* **2021**, *21* (4), 1815−1821.
(55) Chen, C.; Ye, X.; Sun, J.; Chen, Y.; Huang, C.; Xiao, X.; Song, W.; Zhu, S.; Li, T. Bifacial-metasurface-enabled pancake metalens with polarized space folding. *Optica* **2022**, *9* (12), 1314−1322.
(56) Butt, N.; Kim, J.; Mahmood, N.; Park, Y.; Kang, D.; Gao, D.; Zubair, M.; Tauqeer, T.; Mehmood, M. Q.; Gao, L.; Rho, J. Polarization-Controlled Multifunctional Metasurfaces for Ultraviolet-Visible Dual-Band Imaging. *Adv. Funct. Mater.* **2025**, *35* (7), 2410512.
(57) Badloe, T.; Kim, I.; Kim, Y.; Kim, J.; Rho, J. Electrically Tunable Bifocal Metalens with Diffraction-Limited Focusing and Imaging at Visible Wavelengths. *Adv. Sci.* **2021**, *8* (21), 2102646.
(58) Huo, P.; Zhang, C.; Zhu, W.; Liu, M.; Zhang, S.; Zhang, S.; Chen, L.; Lezec, H. J.; Agrawal, A.; Lu, Y.; Xu, T. Photonic Spin-Multiplexing Metasurface for Switchable Spiral Phase Contrast Imaging. *Nano Lett.* **2020**, *20* (4), 2791−2798.
(59) Kim, Y.; Lee, G.-Y.; Sung, J.; Jang, J.; Lee, B. Spiral Metalens for Phase Contrast Imaging. *Adv. Funct. Mater.* **2022**, *32* (5), 2106050.
(60) Zhang, Y.; Lin, P.; Huo, P.; Liu, M.; Ren, Y.; Zhang, S.; Zhou, Q.; Wang, Y.; Lu, Y.-q.; Xu, T. Dielectric Metasurface for Synchronously Spiral Phase Contrast and Bright-Field Imaging. *Nano Lett.* **2023**, *23* (7), 2991−2997.
(61) Badloe, T.; Kim, Y.; Kim, J.; Park, H.; Barulin, A.; Diep, Y. N.; Cho, H.; Kim, W.-S.; Kim, Y.-K.; Kim, I.; Rho, J. Bright-Field and Edge-Enhanced Imaging Using an Electrically Tunable Dual-Mode Metalens. *ACS Nano* **2023**, *17* (15), 14678−14685.
(62) Wang, S.; Li, L.; Wen, S.; Liang, R.; Liu, Y.; Zhao, F.; Yang, Y. Metalens for Accelerated Optoelectronic Edge Detection under Ambient Illumination. *Nano Lett.* **2024**, *24* (1), 356−361.
(63) Sun, C.; Pi, H.; Kiang, K. S.; Yan, J.; Ou, J.-Y. Near-Infrared Metalens Empowered Dual-Mode High Resolution and Large FOV Microscope. *Adv. Opt. Mater.* **2024**, *12* (21), 2400512.
(64) Ye, X.; Qian, X.; Chen, Y.; Yuan, R.; Xiao, X.; Chen, C.; Hu, W.; Huang, C.; Zhu, S.; Li, T. Chip-scale metalens microscope for wide-field and depth-of-field imaging. *Adv. Photonics* **2022**, *4* (4), No. 046006.

https://doi.org/10.1021/acs.nanolett.5c00695
Nano Lett. XXXX, XXX, XXX−XXX